The Astrophysical Journal, 701:1753–1764, 2009 August 20 doi:10.1088/0004-637X/701/2/1753

OBSERVATIONAL EVIDENCE ON THE PRESENCE OF AN OUTER REFLECTING BOUNDARY IN SOLAR ENERGETIC PARTICLE EVENTS

Lun C. Tan[1,4], Donald V. Reames[1,5], Chee K. Ng[1,4], Oskari Saloniemi[2], and Linghua Wang[3,6]
[1] NASA Goddard Space Flight Center, Greenbelt, MD 20771, USA; ltan@mail.umd.edu
[2] Department of Physics and the Väisälä Institute for Space Physics and Astronomy, University of Turku, Turku, Finland
[3] Space Science Laboratory, University of California, Berkeley, California, CA 94720, USA
Received 2009 November 19; accepted 2009 June 26; published 2009 August 4

ABSTRACT

We have focused primarily on the 2001 September 24 solar energetic particle (SEP) event to verify previous indications of the presence of an outer reflecting boundary of SEPs. By using energetic electron and ion data obtained from multi-spacecraft observations, we have identified a collimated particle beam consisting of reflected particles returning from an outer boundary. The peak of reflected particles appears before the arrival of particles at 90° pitch angle. In addition, an onset time analysis is carried out in order to determine parameters characterizing the boundary. Our analysis suggests that the presence of a counter-streaming particle beam with a deep depression at ∼90° pitch angle during the onset phase is evidence for a nearby reflecting boundary. We have compared this property in the SEP events of 2002 April 21 and August 24. A reflecting boundary that blocks a flux tube is important in space weather forecasting since it can cause the "reservoir" effect that may enhance the intensity and duration of high-energy particles.

Key words: acceleration of particles – interplanetary medium – shock waves – Sun: coronal mass ejections (CMEs) – Sun: particle emission

1. INTRODUCTION

1.1. Recent Progress in Investigating Outer Reflecting Boundary of SEPs

Our investigation of an outer reflecting boundary of solar energetic particles (SEPs) began with an ion anisotropy analysis (Tan et al. 2007) that provided an independent way to examine the high-energy variability in SEP events, an outstanding issue in solar-terrestrial physics. In the analysis of 2–8 MeV nucleon^{-1} ion data from the *Wind*/Low-Energy Matrix Telescope (LEMT; von Rosenvinge et al. 1995) in some large SEP events we observed a flow reversal of heavy ions, while protons maintained their flow direction continuously.

A likely explanation of the heavy-ion flow direction reversal was that, in the given MeV nucleon^{-1} range, softening ion spectra at local interplanetary (IP) shock caused the shock to effectively accelerate more protons than heavy ions (see Desai et al. 2003, 2004; Tylka et al. 2005, 2006). Consequently, heavy ions predominantly come from early acceleration near the Sun. Reflection of the heavy-ion-rich material beyond 1 AU can cause a flow reversal of the ions at 1 AU. During some events with consecutive coronal mass ejections (CMEs), there is evidence (Bieber et al. 2002; Reames & Ng 2002; Tan et al. 2007) of a nearby reflecting boundary of SEPs. In fact, downstream of an IP shock driven by a CME, a magnetic mirror can be formed in the bottleneck of magnetic field lines draped around the west flank of the CME (Tan et al. 1992; Bieber et al. 2002). The magnetic bottleneck plays a role of the outer reflecting boundary for SEPs.

Subsequently, we examined the effect of boundary reflection on the high-energy variability of particles in large SEP events. It is known that often two "gradual" SEP events having very similar solar progenitors show similar characteristics at ion energies less than ∼10 MeV nucleon^{-1}, but at higher energies exhibit large difference in their abundance ratio, event size, spectral shape, GeV-ion content, and event duration (Reames 1999; Tylka et al. 2005, 2006). Tylka et al. (2006) and Tylka & Lee (2006) attributed the difference to the interplay between two factors: the evolution in geometry of CME-driven shocks and the seed population consisting of both solar-wind suprathermals and impulsive flare suprathermals. While particle reflection at a boundary beyond 1 AU is unlikely to influence shock acceleration close to the Sun (and hence the original magnitude of particle abundance ratios), we suggested that a boundary that "blocks" a flux tube would increase the intensity and duration of high-energy particles inside the tube, leading to the so-called reservoir effect (Roelof et al. 1992; Reames et al. 1996). Consequently, time and energy changes in particle ratios would occur in association with the existence of the boundary.

In order to verify the reservoir effect caused by a boundary, in Tan et al. (2008) we re-analyzed the famous event pair (the 2002 April 21 and August 24 events) previously examined by the Solar, Heliospheric, and Interplanetary Environment (SHINE) workshop campaign (see http://cdaw.gsfc.nasa.gov/SHINE_Campaign/index.html). The April and August events were similar in flare location, CME speed, and solar wind and IP shock condition. The event duration of >100 MeV protons in the April event, however, was ∼10 times longer than that in the August event. Through our analysis (see Tan et al. 2008), we observed that in the April event the field-aligned component of first-order anisotropy of heavy ions in the solar-wind frame showed a streaming reversal, while in the August event no streaming reversal was seen. Thus, observations on both event duration and streaming reversal of SEPs consistently indicate the presence and absence of the boundary in the April and August events, respectively. In addition, the boundary difference in the two events is supported by IMF and solar-wind measurements. We also observed a temporal variation of Fe/O ratios in association with the presence of the boundary (Tan et al. 2008).

[4] Also at Department of Astronomy, University of Maryland, College Park, MD 20742, USA.
[5] Also at Institute for Physical Science and Technology, University of Maryland, College Park, MD 20742, USA.
[6] Also at Physics Department, University of California, Berkeley, California, CA 94720, USA.

1.2. Can We Confirm the Presence of the Boundary?

So far the presence of a nearby outer reflecting boundary of particles in large SEP events has only been a hypothesis that was introduced to mainly explain the observed streaming reversal of heavy ions. However, we could not confirm the presence of the boundary by identifying a particle beam consisting solely of reflected ions due to the interference of scattered particles that quickly mask the distribution of reflected particles.

Since the accumulated variation of particle pitch-angle distributions is the integrated effect of particle scattering probability over the elapsed time interval, longer delay after the event onset would result in greater scattering of the particles. Therefore, in order to diminish the influence of scattered particles, we might consider using higher-speed particles (both electrons and ions) that arrive at 1 AU within a shorter time. In effect, since the mean free path of ions is an increasing function of ion rigidity (e.g., Dröge 2000), we prefer to sample higher-rigidity ions in order to verify the presence of a reflected beam.

1.3. Why Do We Select the 2001 September 24 Event as Our Target?

Energetic electron anisotropy data measured by the *Wind*/3-Dimensinonal Plasma (3DP) Analyzer (Lin et al. 1995) are available for the September event. However, since there are few proton anisotropy measurements at the proton kinetic energy $T > 20$ MeV, we checked the availability of proton anisotropy data in the September event. Potentially, there are proton data from the IMP-8/Goddard medium energy detector (MED; McGuire et al. 1986) and the *SOHO*/Energetic and Relativistic Nuclei and Electron (ERNE) sensor (Torsti et al. 1995). Since the IMP-8/MED data only show a continuous coverage of individual SEP events during earlier years of operation, they rarely provide data for SEP events detected by the *Wind*/LEMT sensor. On the other hand, since the *SOHO*/ERNE sensor was designed for low solar activity periods, it is easily saturated in large SEP event. Fortunately, we have identified SEP events, in which no saturation of high-energy proton intensities occurred during the first few hours from event onset. Among them is the 2001 September 24 event previously examined in Tan et al. (2007, 2008). The absence of saturation in the September event is probably due to the relatively slow increase of proton intensities in this E23 flare associated event.

Furthermore, we have noted that the September event had a "clear" IP environment; especially in the sense that there was only one preceding CME (CME1) ahead of the primary CME (CME2), making it easier to determine the likely location of the reflecting boundary. In fact, we associate the reflecting boundary with Shock1 prior to CME1, which has a postshock velocity of $V_{sw1} \sim 600$ km s^{-1}. Assuming the average CME1 speed between the Sun and 1 AU was between V_{sw1} and 3 V_{sw1}, CME1 would be launched between September 20 12:00 (UT) and September 22 10:00 (UT). During this time interval, 16 CME events were observed. Only one had linear speed (659 km s^{-1}) greater than 600 km s^{-1} and it is identified as CME1.

In addition, from the observation by the *SOHO*/Large Angle and Spectrometric Coronagraph (LASCO) telescope (http://cdaw.gsfc.nasa.gov/CME_list), we obtain the onset time of a CME by extrapolating its height–time plot to the solar surface. The onset times of CME1 and CME2 are 09:05:28 and 10:21:03 (UT), respectively, for linear height–time fits, and 08:04:08 and 10:19:21 (UT), respectively, for quadratic height–time fits. (Note that the CME launch time quoted in Tan et al. (2008) was actually the extrapolated to $t = 0$ time of its height–time plot). Also, the *Wind* spacecraft observed the IP shock (Shock1) prior to CME1 at September 23 09:18 (UT), and the solar-wind speed after Shock1 was ~580 km s^{-1}. Therefore, at the launch time of the primary CME (CME2), the estimated radial distance of the leading edge of the preceding CME1 was ~1.3 AU, implying the possible presence of a nearby outer reflecting boundary.

1.4. Questions to be Addressed in This Work

We wish to verify the presence of a nearby outer reflecting boundary of SEPs in the September event by using energetic electron and ion data obtained from multi-spacecraft observations. The first question we will address is whether, based on electron and ion anisotropy data, we can identify a particle beam solely consisting of reflected particles, and hence confirm the presence of the boundary that reflected these particles back to 1 AU. Given a confirmation of a boundary, our second question will be what parameters of the boundary can be extracted from the analysis of both incident and reflected particle beams. Is the parameter estimation from electron data consistent with that from ion data? How did both incident and reflected particle beams evolve with time? Finally, our third question will be whether in large SEP events we can find a condition to discriminate between the presence and absence of a boundary. Since the existence of the boundary would cause a reservoir effect that may enhance the intensity and duration of high-energy particles, such condition is important for space weather forecasting.

Data from the *Wind* and *SOHO* spacecraft are used in this work. We first present the evidence for the presence of an outer reflecting boundary in the September event. Then, through the onset time analysis, we determine parameters characterizing the boundary. Finally, we explain why the depression of 90° pitch-angle particles could be a strong evidence to discriminate between the existence and absence of the boundary and we revisit the 2002 April and August events using electron anisotropy data.

2. OBSERVATIONS

2.1. Observed Data

In addition to the *Wind*/LEMT ion data used in our previous work (Tan et al. 2007, 2008), electron data from the *Wind*/3DP sensor and proton data from the *SOHO*/ERNE sensor are also used in the present work.

The *Wind*/3DP semiconductor detector telescope (SST) includes the electron foil instrument consisting of six telescopes each with the field of view of 36° × 20° (Lin et al. 1995). It measures the electron energy of $T_e = 25$–400 keV with a full 4π angular coverage in one spacecraft spin period (3 s). The data measured by the SST instrument are sorted into 48 angular bins, each roughly has a 36° × 22.°5 resolution. Using magnetic field data from the WIND/Magnetic Field Instrument (MFI), the electron data stored in two-dimensional (2D) angular bins are again sorted into eight one-dimensional (1D) pitch-angle sectors having a 22.°5 resolution. Each sector is labeled by its averaged pitch-angle value. The time resolution of the *Wind*/3DP data used by us is 12 s. In SST, a fraction of incident electrons would scatter out and deposit only part of their energy at channels lower than the incident energy. In this study, this contamination has been removed.

The *SOHO*/ERNE high-energy detector (HED) provides proton intensity data with high sensitivity in the proton kinetic

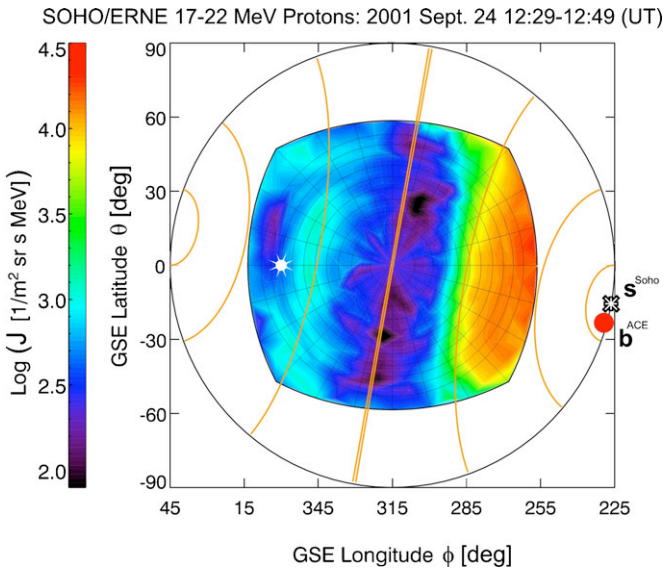

Figure 1. View-cone schematic of *SOHO*/ERNE 17–22 MeV protons during 12:29–12:49 (UT), 2001 September 24. Since the origin of the view cone is at the nominal Parker spiral direction (i.e., $\phi = 315^\circ$ and $\theta = 0^\circ$ in the GSE system), the Sun (white star) is at 45° left from the center. The red dot and white cross are the magnetic field direction measured by *ACE* and symmetric axis of *SOHO* proton pitch-angle distributions, respectively.

energy range of T = 12–140 MeV. The sensor utilizes 241 solid-angle elements to record the unidirectional proton intensity J. Since there is no MFI aboard *SOHO*, the pitch angle α of detected protons is calculated with respect to the magnetic field direction measured on the *ACE* spacecraft. The resulting uncertainty of *SOHO* proton pitch-angle distributions is analyzed in the Appendix. The time resolution of the *SOHO*/ERNE data used by us is 12 minutes.

Unlike *Wind*, the *SOHO* spacecraft does not spin. The *SOHO*/ERNE experiment has a central axis aligned with the nominal Parker spiral direction, and a rectangular aperture collecting particles arriving from directions up to 60°–68° from the sensor axis. Therefore, if the magnetic field is along the nominal Parker spiral direction, the sensor only samples protons with pitch angle $\alpha < 68^\circ$. However, since the magnetic field is nearly perpendicular to the Parker spiral direction during the September event period (Tan et al. 2007), the sensor is accurate in measuring protons with $\alpha \sim 90^\circ$ (i.e., the pitch-angle cosine $\mu = \cos(\alpha) \sim 0$).

The pitch-angle coverage of the *SOHO*/ERNE sensor can be seen in its view-cone schematic (Figure 1), which is a hemisphere in the GSE system centered at the nominal Parker spiral direction (i.e., GSE longitude $\phi = 315^\circ$ and latitude $\theta = 0^\circ$). Thus, the Sun (the white star) is at 45° left from the center, and the unit vector $\mathbf{b}^{ACE}$ (the red dot), along the magnetic field direction measured by the *ACE* spacecraft, is ~90° right because the field is nearly perpendicular to the Parker spiral. From Figure 1, it can be seen that during the September event period the *SOHO*/ERNE sensor had a coverage of $150^\circ > \alpha > 30^\circ$ (i.e., $-0.87 < \mu < 0.87$), restricting its ability to detect protons at $|\mu| \sim 1$.

2.2. Pitch-angle Distribution of SEPs

2.2.1. Pitch-angle Distributions of Wind/3DP Energetic Electrons

Energetic electrons are suitable for examining the reflecting boundary of SEPs because of their high speed. In fact, electrons

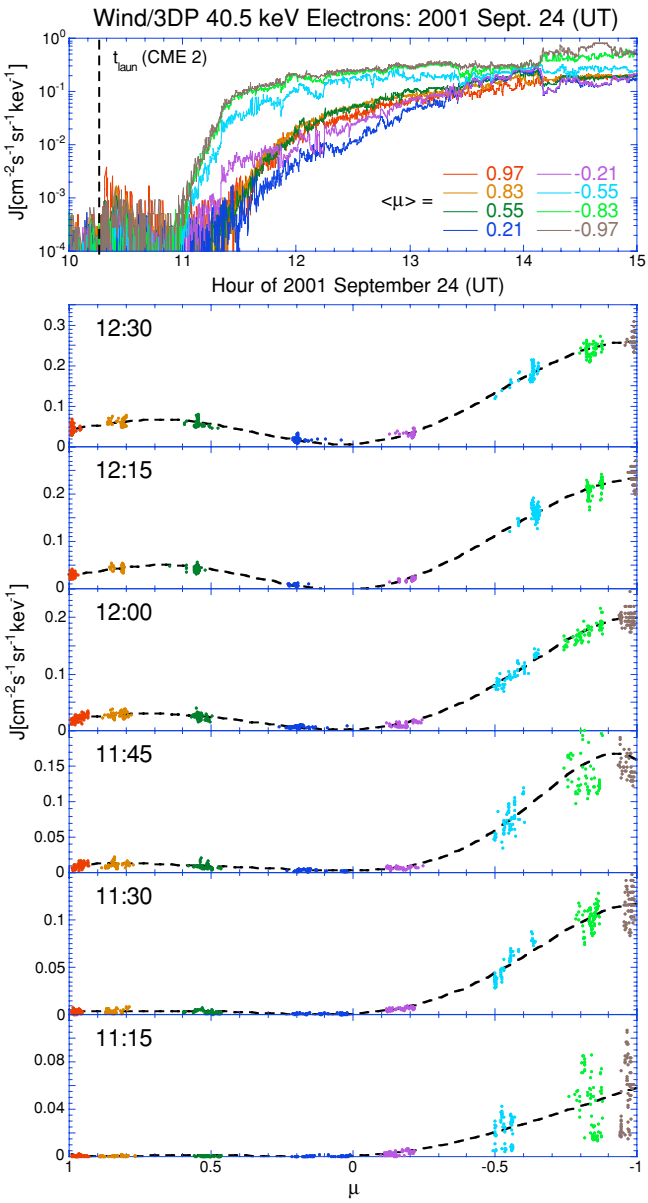

Figure 2. Top panel: time profiles of the unidirectional differential intensity (J) of *Wind*/3DP 40 keV electrons at different mean pitch-angle cosine ($\langle\mu\rangle$) values. Lower panels: plot of J vs. μ for different time intervals in the 2001 September 24 event. Hereafter, the time interval is counted from bottom to top with the start time of each interval displayed.

with T_e = 21.8 keV have a speed as same as protons with T = 40 MeV. The pitch-angle distributions of 40 keV electrons measured by the *Wind*/3DP sensor are shown in Figure 2, where the top panel presents the time profiles of J at different mean $\langle\mu\rangle$ values. Since the relative magnitude of J among different $\langle\mu\rangle$ values varies with time, we plot J against μ for each 15 minute interval in the remaining panels of Figure 2, where the time interval is counted from bottom to top with the starting time of each interval indicated.

Here, we explain how the pitch-angle distribution (i.e., J as a function of μ) in Figure 2 is generated. As described earlier, the electron intensity J recorded in 2D angular bins is sorted to the 1D pitch-angle sector having an angular width of 22.5. Thus, the final pitch-angle distribution consists of eight sectors, whose central value is $\alpha_0(j) = 11.25 + 22.5 \times (j - 1)$ (°), where $j = 1, 8$. On average, there are $48/8 = 6$ angular

bins entering into one sector. We hence need to calculate the electron intensity (J_m) and pitch-angle (α_m) values averaged over a sector. Because of the time variation of the magnetic field direction, the angular bins entering into a given pitch-angle sector (j) are time dependent, leading to the time dependence of $\alpha_m(j)$ value. The $\alpha_m(j)$ value is different from the nominal value $\alpha_0(j)$, although the difference between them is less than the α_0 difference between two adjacent sectors.

Furthermore, over a 15 minute sampling interval, we plot on the same panel all of *Wind*/3DP pitch-angle distributions that have a 12 s time resolution. Thus, there are $15 \times 60/12 = 75$ observed J_m versus α_m data points shown in one pitch-angle sector. Since these data points tend to be concentrated near α_0, there are gaps in the observed pitch-angle distribution. Nevertheless, the gaps do not affect the examination of the global characteristics of the distribution. Also, since there are a lot of data points crowded within one pitch-angle sector, for clarity we have ignored their error bar plotting. Note that the error of μ is $\sigma_\mu = \sin(\alpha)\sigma_\alpha$, where the error of α is $\sigma_\alpha = 11.^\circ25$, i.e., one half of the angular resolution of *Wind*/3DP data (Wang et al. 2006).

At the first stage during the event onset, there were only incident electrons at $\mu < -0.2$. Later, an electron intensity peak began to appear at $\mu \sim 0.7$, while 90° pitch-angle electrons (at $\mu \sim 0$) were still absent. Since incident electrons were limited at $\mu < -0.2$, the scattering of incident electrons would first enhance the intensity at $\mu \sim 0$. The dearth of electrons at $\mu \sim 0$ indicates that the electron peak at $\mu \sim 0.7$ consists solely of reflected electrons. In addition, it can be seen that the intensity at $\mu \sim 1$ is less than the peak intensity of reflected electrons, indicating the deficiency of electrons there, which is consistent with the presence of loss cone at the magnetic mirroring point (e.g., Bieber et al. 2002).

2.2.2. Pitch-angle Distribution of *SOHO*/ERNE High-energy Protons

At the onset of the September event, the *SOHO*/ERNE proton pitch-angle distribution at $T = 28$–54 MeV is shown in Figure 3, where the time resolution of $J(\mu)$ data is 12 minutes except for the bottom panel that shows the pre-event background proton intensity with a time resolution of 24 minutes.

It should be noted that μ in the *Wind*/3DP data is defined by using the particle flow direction with respect to the magnetic field, while μ in the *SOHO*/ERNE data is defined by using the detector pointing direction with respect to the magnetic field. Since the detector pointing direction is *against* the particle flow direction, there is a sign reversal of μ between the two sensors. In view of the difficulty to unify the definition of μ in the two data sets, we have adjusted the orientation of X-axis, so that the incident particle beam always appears on the right side of a figure.

The behavior of the *SOHO*/ERNE proton data shown in Figure 3 is very similar to that of the *Wind*/3DP electron data shown in Figure 2. In particular, at the event onset, incident protons were only observed at $\mu > 0.3$. Later, a peak of reflected protons appeared at $\mu = -0.6$ to –0.7. Since the peak of the reflected protons appears before the arrival of 90° pitch-angle protons, both *Wind*/3DP electron and *SOHO*/ERNE proton data have confirmed the presence of an outer reflecting boundary of SEPs.

Let us compare the scattering probability of protons with that of electrons. From Figures 2 and 3, it can be seen that the widths of both incident and reflected particle beams of $T_e = 40$ keV ($R_e = 0.206$ MV) electrons are wider than those of $T = 40$ MeV

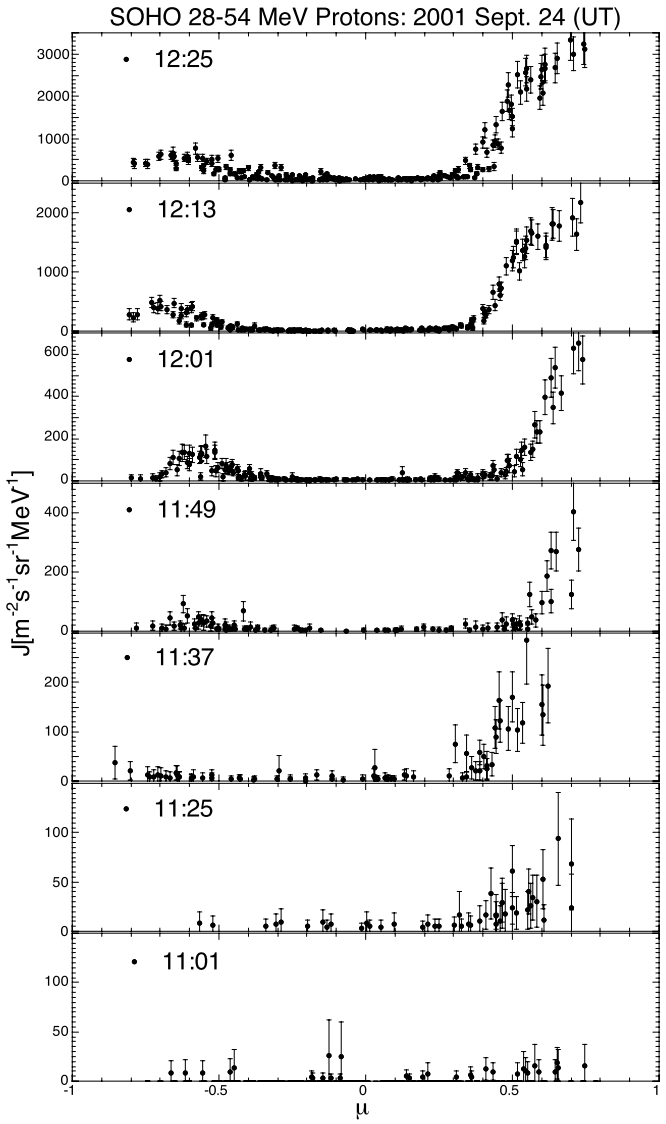

Figure 3. Plot of J vs. μ for the *SOHO*/ERNE 28–54 MeV protons in the 2001 September 24 event.

($R = 277$ MV) protons (although the speed of $T_e = 40$ keV electrons is greater than $T = 40$ MeV protons), indicating that the scattering probability of the $T_e = 40$ keV electrons is greater than that of $T = 40$ MeV protons.

SOHO/ERNE proton intensity data at lower energies ($T = 17$–22 MeV) are shown in Figure 4, where the influence of proton scattering is more obvious. Nevertheless, the peak of reflected protons was still visible during the time interval of 12:35–12:59 (UT). Thus, the existence of reflected proton beam in the September event is also confirmed by these lower energy proton observations.

Since the arrival of reflected protons was earlier than protons at $\mu \sim 0$, it is interesting to examine the way both extremely anisotropic beams of incident and reflected protons evolved to a nearly isotropic proton distribution. Hence, we plot the pitch-angle distribution of *SOHO*/ERNE 28–54 MeV protons in Figure 5 during a time interval following that shown in Figure 3. It can be seen that as the peak intensity of reflected protons increased, the width of their distributions also increased. Finally, the $\mu \sim 0$ region was predominantly filled by reflected protons.

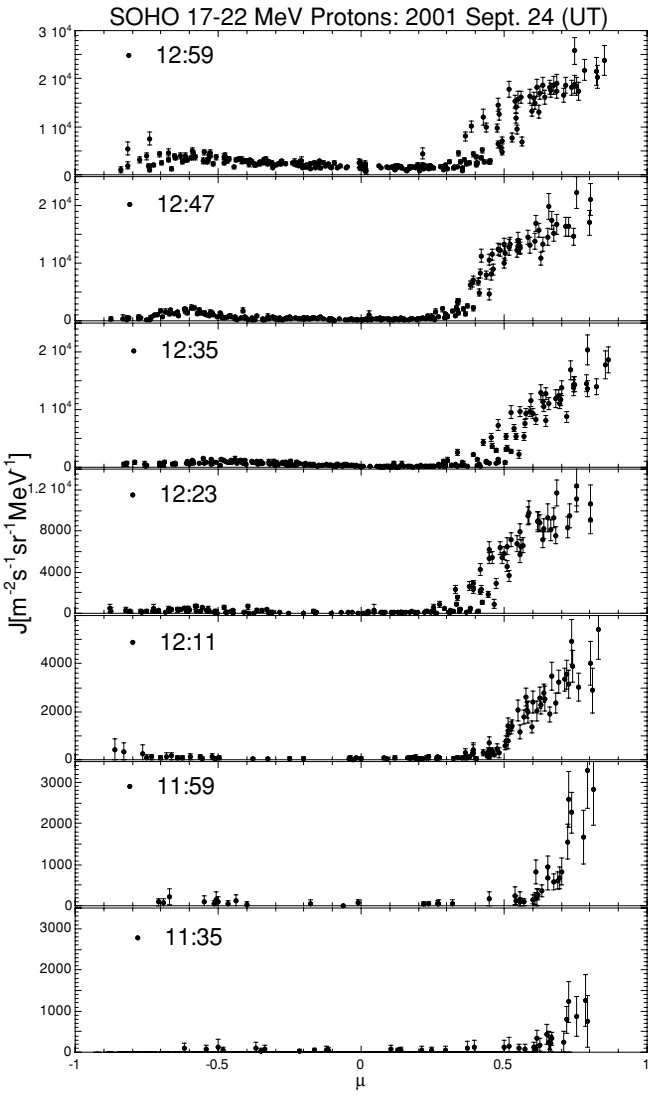

Figure 4. Same as Figure 3, but for the *SOHO*/ERNE 17–22 MeV protons.

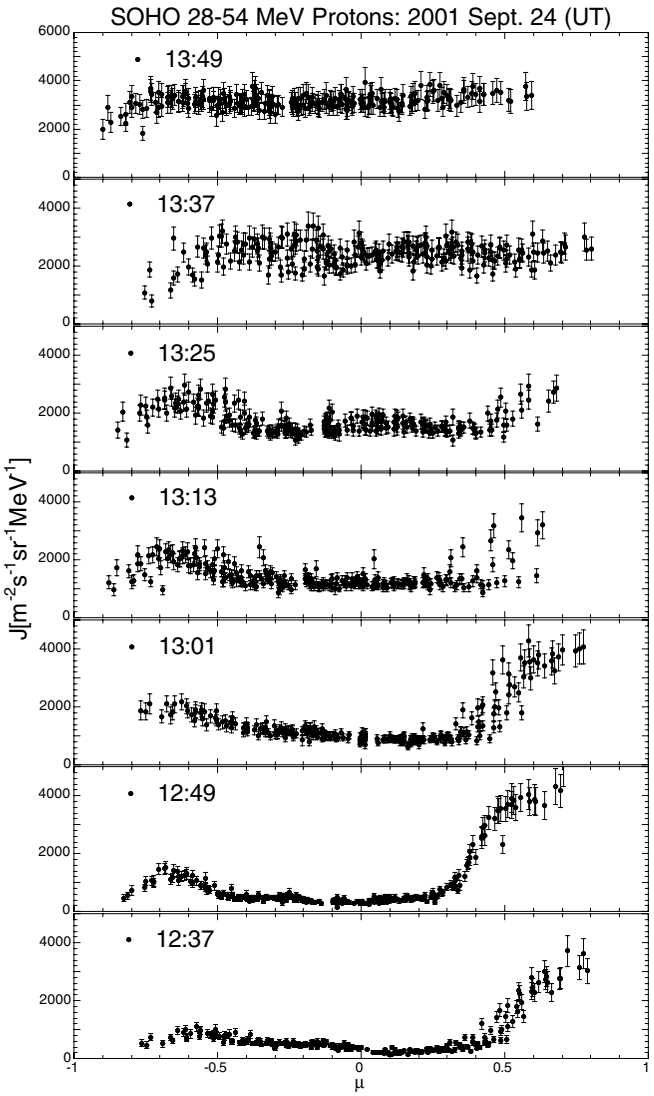

Figure 5. Same as Figure 3, but for the time period following that in Figure 3.

2.3. Onset Time Analysis of SEPs

2.3.1. Velocity Dispersion Relationship

Assuming that the first returning reflected particles have experienced negligible scattering, the location of the outer reflecting boundary of SEPs can be determined by measuring the transport time of particles. There are two epochs: the time the incident particles arrive at 1 AU, t_i, and the time the reflected particles return to 1 AU, t_r.

For t_i values of various particles, the velocity dispersion relationship, that higher-speed particles arrive at 1 AU earlier than lower-speed particles, allows us to determine the solar release time t_0 and the path length L_0 traveled by first arriving particles from the Sun to 1 AU, i.e.,

$$t_i = t_0 + L_{0i}/v, \tag{1}$$

where the subscript i in L_0 indicates incident particles, assuming that first arriving particles have $\mu = 1$ (Tylka et al. 2003; Mewaldt et al. 2003; Reames 2009). For impulsive SEP events, Tylka et al. (2003) found that the solar release time of the particles was in excellent agreement with the hard X-ray peak, proving the validity of the technique. Reames (2009) discussed reasons that the limitations imposed by scattering calculations appear to be overestimated. Like Tylka et al. (2003), Reames (2009) found the same velocity dispersion, path lengths, and release times for different particle species that might be expected to have different scattering mean free paths.

For t_r values, the situation is somewhat different. Since at the magnetic mirroring point the incident protons inside the loss cone cannot be reflected back to 1 AU, most of the particles that first reach the reflecting boundary would be lost. Only a small portion of particles outside the loss cone that escape scattering into the loss cone can return to 1 AU. These particles would be mainly located at the peak of reflected particles with their pitch-angle cosine μ_m. We hence have

$$t_r = t_i + 2l_m/(\mu_m v), \tag{2}$$

where l_m is the distance from the 1 AU observer to the magnetic mirroring point. Equation (2) can be re-written as the velocity dispersion relationship of reflected particles

$$t_r = t_0 + L_{0r}/v, \tag{3}$$

where the subscript r in L_0 indicates reflected particles. From Equation (2), we have $L_{0r} = L_{0i} + 2l_m/\mu_m$.

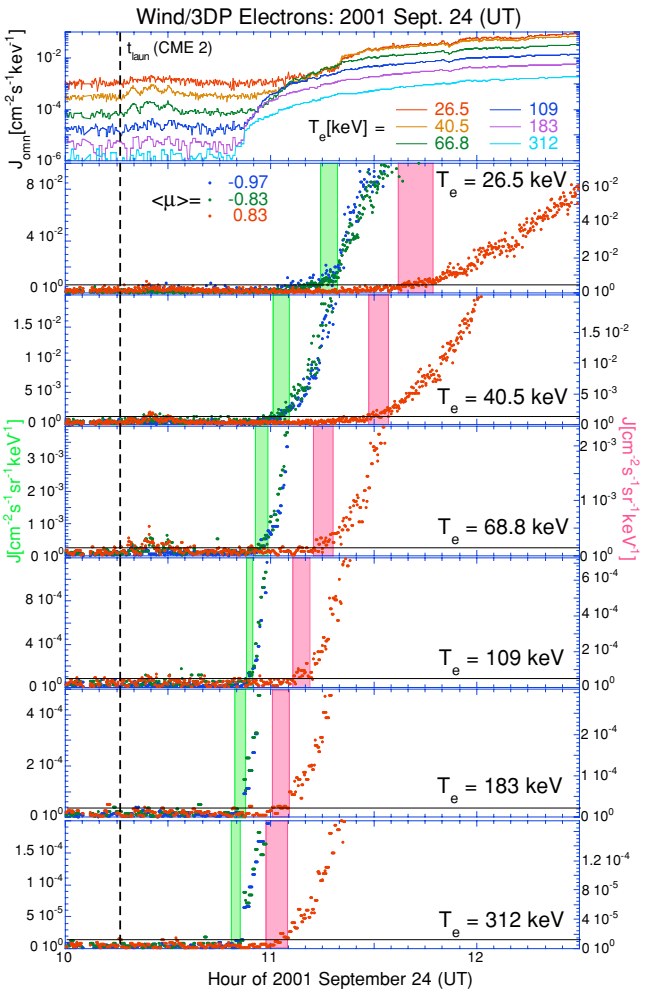

Figure 6. Top panel: time profiles of the omnidirectional intensity ($J_{\rm omn}$) of *Wind*/3DP electrons at different electron energies (T_e). Lower panels: time profiles of the unidirectional intensity (J) of *Wind*/3DP electrons at selected $\langle\mu\rangle$ values for different electron energies (T_e) in the 2001 September 24 event. The horizontal black line is the common 2σ-limit of both incident and reflected electrons. Shaded green and red regions are the estimated time ranges of first arriving at 1 AU incident and reflected electrons, respectively.

2.3.2. Electron Transport Time Observation

We first examine energetic electron data. The time profiles of electron $J_{\rm omn}$ data measured by the *Wind*/3DP sensor at T_e = 25–400 keV are shown in the top panel of Figure 6, where the intensity of background electrons is significant.

Recently, Lintunen & Vainio (2004) and Saiz et al. (2005) examined the "theoretical" uncertainty of the velocity dispersion analysis in the estimation of onset times of SEPs under various assumptions about injection profiles, IP scattering, and detection thresholds. Through simulations, Saiz et al. (2005) noted that under a low-threshold approximation the errors in the estimation of t_0 and L_{0i} would be several minutes and ~0.2 AU, respectively. Because we are interesting in the reflecting boundary location that is deduced from the difference $L_{0r} - L_{0i} = 2l_m/\mu_m$ (see Equation (3)), these theoretical uncertainties should be acceptable. However, the "observational" uncertainty in the velocity dispersion analysis may be more serious. For example, from 80 near-relativistic solar electron events Kahler & Ragot (2006) found that in most cases the inferred $L_{0i} < 1$ AU, which is unphysical and is most likely due to instrumental effects.

The error in identifying electron onset times is probably one of main sources of observational uncertainty, because onset times are always measured under the presence of significant background electron intensity. In fact, according to Tylka et al. (2003) one identifies the onset time by requiring a $\geqslant 2\sigma$ increase (i.e., above the 95 percentile line in Gaussian statistics) of background particle intensity. Assuming that the mean value and standard deviation of background particle intensities preceding the event are, respectively, $J_{\rm mbk}$ and $\sigma_{\rm bk}$, the 2σ-limit is $J_{2\sigma} = J_{\rm mbk} + 2\sigma_{\rm bk}$. Unfortunately, since the background electron intensity is usually time dependent and shows nondispersive variations on different timescales (Kahler & Ragot 2006), it is very difficult to make a reasonable estimation of $J_{2\sigma}$ before the arrival of incident particles.

To our knowledge, previous studies have determined onset times using the omnidirectional electron intensity ($J_{\rm omn}$) data. The initial rate of rise is generally slower in $J_{\rm omn}$ than in the directional intensity, $J(|\mu| \sim 1)$. One factor that enhances the reliability of the onset determination is having a sharp rise out of background (Lintunen & Vainio 2004; Saiz et al. (2005)). In this study, we therefore undertake the onset analysis using the directional flux $J(|\mu| \sim 1)$.

We have used the electron-scattering-corrected *Wind*/3DP $J(|\mu| \sim 1)$ data to improve the estimation of 2σ-limit. We find that the ratio $J_{2\sigma i}/J_{2\sigma r}$, where $J_{2\sigma i}$ and $J_{2\sigma r}$ are, respectively, the $J_{2\sigma}$ values of incident and reflected electrons, is nearly time independent. We hence plot the incident and reflected electron intensities in Figure 6 by using the left (Y_i) and right (Y_r) vertical axes, respectively. In the figure, $\langle\mu\rangle = -0.97$ and -0.83 indicate incident electrons, while $\langle\mu\rangle = 0.83$ shows reflected electrons. The agreement between the $\langle\mu\rangle = -0.97$ and -0.83 channels is probably due to the wide angular resolution of the *Wind*/3DP sensor that first arriving electrons with $\mu \sim -1$ could also be detected by the sector with $\langle\mu\rangle = -0.83$. Also, pitch-angle scattering of electrons through the IP medium may disperse electrons from $|\mu| \sim 1$ into smaller $|\mu|$. The use of the two channels is in order to enhance the statistics of incident electrons.

We then set the limits of Y_i and Y_r axes at J_i and J_r, respectively. Assuming that $J_i/J_r = J_{2\sigma i}/J_{2\sigma r}$, the 2σ-limits of both incident and reflected electrons would have the same height as shown in Figure 6 by the horizontal black line. This "normalized" 2σ-limit is helpful in identifying the first arriving time of electrons, because the interference of background electron intensity variations with shorter timescales can be reduced (see T_e = 68.8 keV channel after $t_{\rm laun}$(CME2)). The onset time ranges thus determined for both incident and reflected electrons are shown in Figure 6 as the shaded green and red regions, respectively. Based on these measurements, we carry out the velocity dispersion analysis of electrons later.

2.3.3. Ion Transport Time Observations

2.3.3.1. Time of Incident Ion Arrival at 1 AU t_i

Figure 7 shows the ion onset time data collected from the *Wind*/LEMT and *SOHO*/ERNE sensors. In the top panel, the time profiles of $J_{\rm omn}$ for H and He ions at different ion energies are plotted with a time resolution of 5 minutes on a linear scale. Because of the negligible background, it is not difficult to determine the t_i value of these ions.

We then examine intensity data of *SOHO*/ERNE high-energy protons without background subtraction in the second panel. Because of the limited pitch-angle coverage in the *SOHO*/ERNE sensor (see Figure 1), there was no nominal μ ~1 data

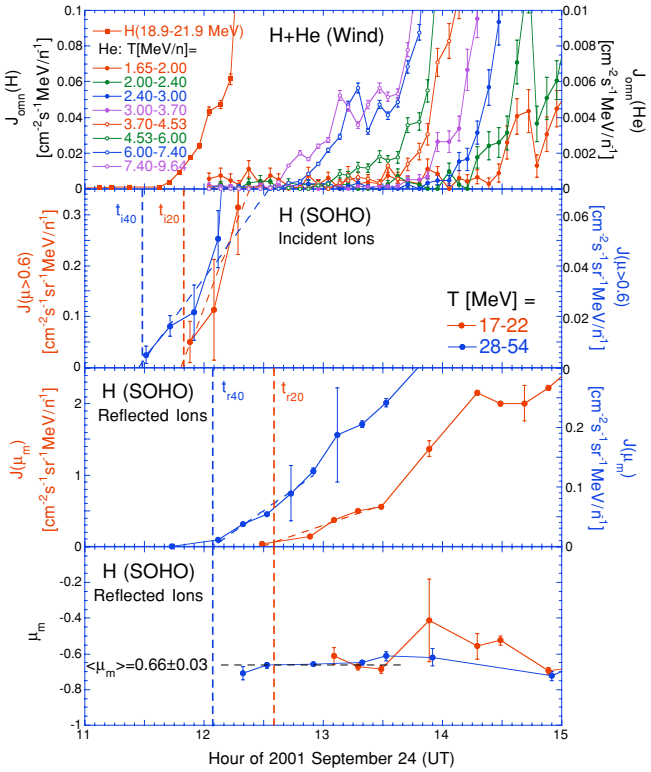

Figure 7. Time profiles of $J_{\rm omn}$ of H, He ions deduced from the *Wind*/LEMT data (top panel), $J(\mu > 0.6)$ of protons from the *SOHO*/ERNE data (second panel), $J(\mu_{\rm m})$ measured at the intensity peak of reflected protons (third panel), and the μ_m value of the reflected proton intensity peak (bottom panel) from the *SOHO*/ERNE data. The vertical dashed lines t_i and t_r show the estimated times of first arriving at 1 AU incident and reflected protons, respectively.

during the September event period. Nevertheless, we may use the proton intensity data at $\mu > 0.6$ (i.e., J ($\mu > 0.6$)) to estimate t_i of incident protons. Owing to the lack of magnetic field measurement aboard *SOHO* (see the Appendix), the J ($\mu > 0.6$) data may contain a significant fraction of $\mu \sim 1$ protons. In fact, from Figure 12, it can be seen that with a nominal value of $\mu = 0.75$ the $\pm 3\sigma$-limit of μ is 0.50–0.93, indicating the presence of first arriving protons with $\mu \sim 1$ in J ($\mu > 0.6$). We then determine t_i of *SOHO*/ERNE proton data from the sudden increase of J ($\mu > 0.6$) as denoted by the vertical dashed line in Figure 7.

2.3.3.2. *Reflected Ion Returning to 1 AU Time t_r*

We use the unidirectional proton intensity ($J(\mu_m)$) measured at the reflected proton intensity peak, whose pitch-angle cosine is μ_m, to estimate t_r. Both $J(\mu_m)$ and μ_m are obtained from a parabolic fitting of the pitch-angle distribution of reflected protons. In the third and bottom panels of Figure 7, we show the time profiles of $J(\mu_m)$ and μ_m of *SOHO*/ERNE protons, respectively. Here, we use the bootstrap method (Efron & Tibshirani 1991) to calculate the error of the intensity maximum of reflected protons. At each computation, the input proton intensity at a given μ value is set to be a Gaussian deviate (Press et al. 1989) with a mean value equal to the measured intensity and a variance equal to the measured error of intensities. After a large number (>400) of computations, the deduced ensemble average and standard deviation are shown in Figure 7, where a large error bar of $J(\mu_m)$ usually indicates an imperfect peak of reflected protons. We then estimated t_r from the sudden increase of $J(\mu_m)$ as denoted by the vertical dashed line.

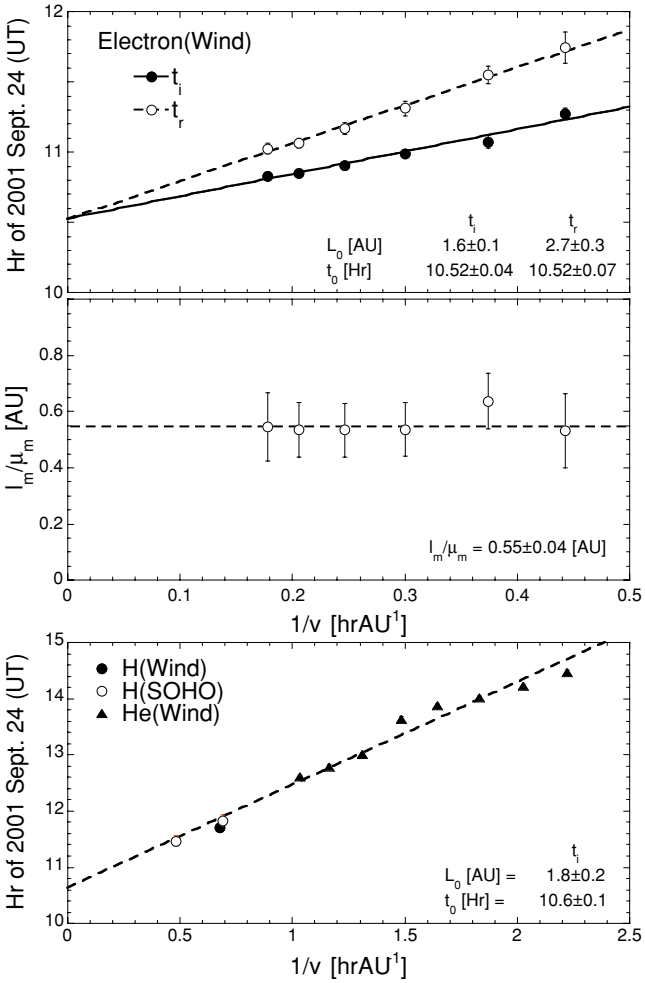

Figure 8. Onset times of electrons (top panel) and distance (l_m) of the magnetic mirroring point to the 1 AU observer (middle panel) as deduced from *Wind*/3DP electron data are plotted against $1/v$, where v is the particle speed. Onset times of H, He ions from *Wind*/LEMT and *SOHO*/ERNE ion data (bottom panel) are plotted against $1/v$. See Figure 7 on the definition of μ_m.

2.3.4. *Results of Onset Time Measurements*

We first examine the velocity dispersion plot of electrons from the *Wind*/3DP data shown in the top panel of Figure 8, where we treated the t_i and t_r data separately. The t_0 values of electrons deduced from t_i and t_r data are 10.52 $\pm$ 0.04 and 10.52 $\pm$ 0.07 (hr) on 2001 September 24 (UT), respectively, well consistent with each other.

We then examine the velocity dispersion plot of H and He ions obtained from the *Wind*/LEMT and *SOHO*/ERNE data shown in the bottom panel of Figure 8. Here, the t_i value deduced from the *Wind*/LEMT $J_{\rm omn}$ point (solid circle) is consistent with that from the *SOHO*/ERNE J ($\mu > 0.6$) data (open circle), justifying our procedure of calculating t_i by using *SOHO*/ERNE J ($\mu > 0.6$) data. The deduced t_0 value of ions is 10.6 $\pm$ 0.10 (hr) on 2001 September 24 (UT), also consistent with that of electrons shown above. The weighted averaged t_0 value of all particle species is 10.53 $\pm$ 0.03 (hr) on 2001 September 24 (UT).

The L_{0i} value deduced from *Wind*/3DP electron data is 1.6 $\pm$ 0.1 (AU), which is also consistent with that deduced from ion data (1.8 $\pm$ 0.2 (AU)). Our deduced L_{0i} value is greater than the length of nominal Parker spiral ($\sim$1.2 AU), which is conceivable in view of the complex-

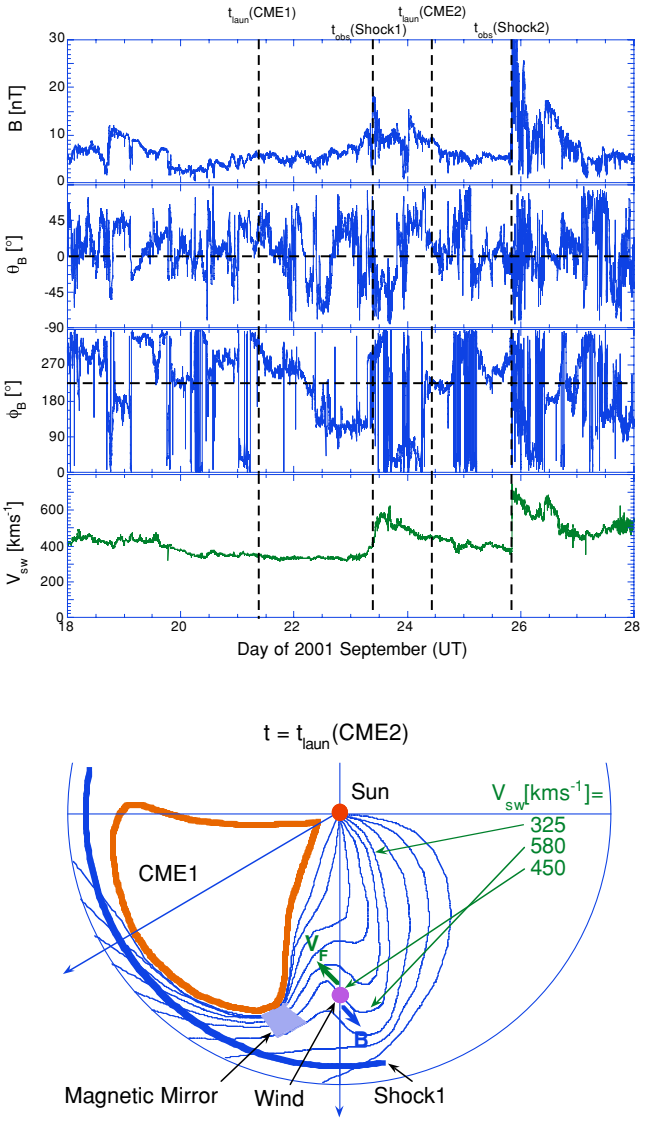

Figure 9. Time profiles of the strength (B, top panel), latitude (θ_B, second panel), and longitude (ϕ_B, third panel) of IMF and the solar-wind speed (V_{sw}, fourth panel) as deduced from *Wind* observations are shown for the 2001 September 24 event. Cartoon to show the effect of high-speed solar-wind stream on ion flow in the 2001 September 24 event (bottom panel).

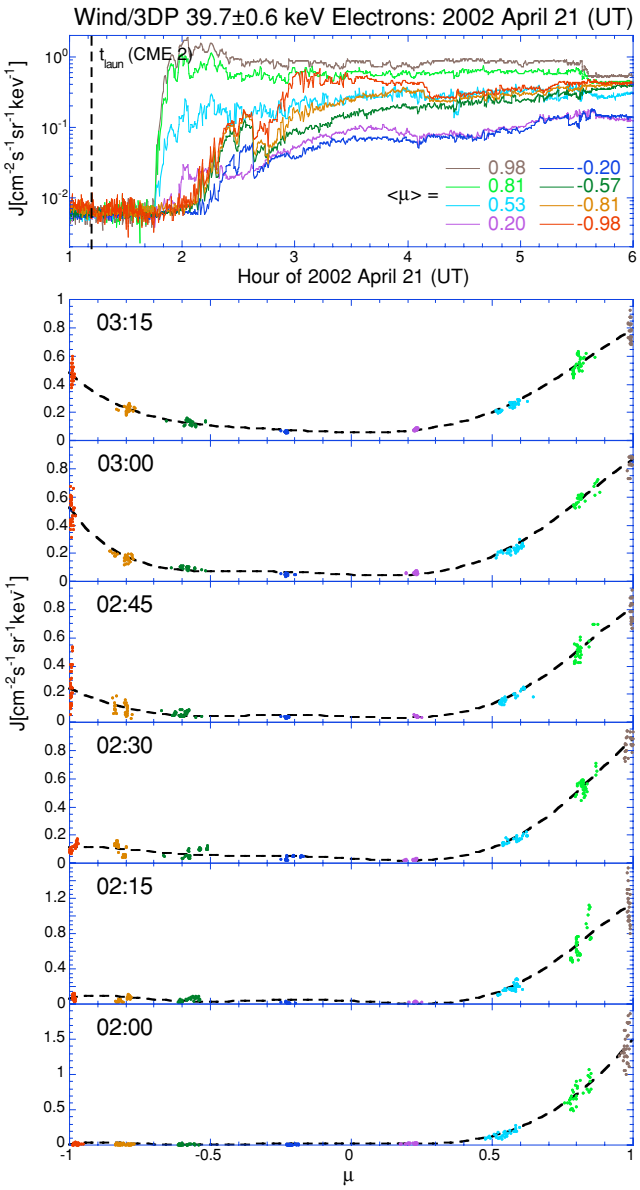

Figure 10. Same as Figure 2, but for the 2002 April 21 event.

ity of magnetic connection in this E23 flare associated event (see Section 3.1).

Finally, based on the speed (2402 km s^{-1}) as well as the launch time of CME2, from our deduced t_0 value, we calculate the release height of SEPs above the Sun. For the September event, the estimated height is 5.0 $\pm$ 0.4 (R_s), where R_s is the solar radius. Very recently, Reames (2009) examined the release height of SEPs in ground-level events. He noted that when the observer is reasonably well connected to the source the height has a fairly narrow range (2–4 R_s), whereas the heights increase at the eastern and western flanks. Our observation is consistent with Reames (2009) because the September event is an E23 event.

2.3.5. Boundary Location Determined from Onset Time Analysis

Onset time analysis can be used to determine characteristic parameters of the magnetic mirroring point. In fact, the conservation of first adiabatic invariant implies $\sin^2(\alpha)/B = \text{constant}$. Assuming that near the magnetic mirroring point the magnetic field strength B abruptly increases from its background value B_{bk} to the maximum value B_m, the loss-cone boundary α_{loss} at 1 AU should be $\sin(\alpha_{loss}) = (B_{bk}/B_m)^{1/2}$. While we cannot directly measure the B_{bk}/B_m value at the mirroring point, we may use the observed B_{bk}/B_m value at 1 AU to approximate it (similar to Bieber et al. 2002). From Figure 9, it can be seen that *Wind* spacecraft recorded $B_m \sim 20$ nT and $B_{bk} \sim 5$ nT after t_{obs}(Shock1). We hence obtain $B_{bk}/B_m \sim 1/4$, $\alpha_{loss} \sim 150°$, and $\mu_{loss} \sim -0.87$. Our estimated μ_{loss} value is consistent with the decrease of J at $\mu < -0.85$ shown in Figure 2.

We then estimate the distance l_m from the observer located at 1 AU to the magnetic mirror point. According to Equation (2), we have $l_m/\mu_m = v\,(t_r - t_i)/2$. From the *Wind*/3DP electron data shown in the middle panel of Figure 8, we obtain $l_m/\mu_m = 0.55 \pm 0.04$ (AU). Also, from the *SOHO*/ERNE proton data shown in Figure 7, we obtain $l_m/\mu_m = 0.6 \pm 0.2$ (AU). Therefore, the final result is $l_m/\mu_m = 0.55 \pm 0.04$ (AU). Since the size of the loss cone only depends on magnetic compression, the location of intensity maximum of reflected particles should be independent of the nature of particles. Owing to $\langle\mu_m\rangle = 0.66 \pm 0.03$ deduced from the *SOHO*/ERNE proton

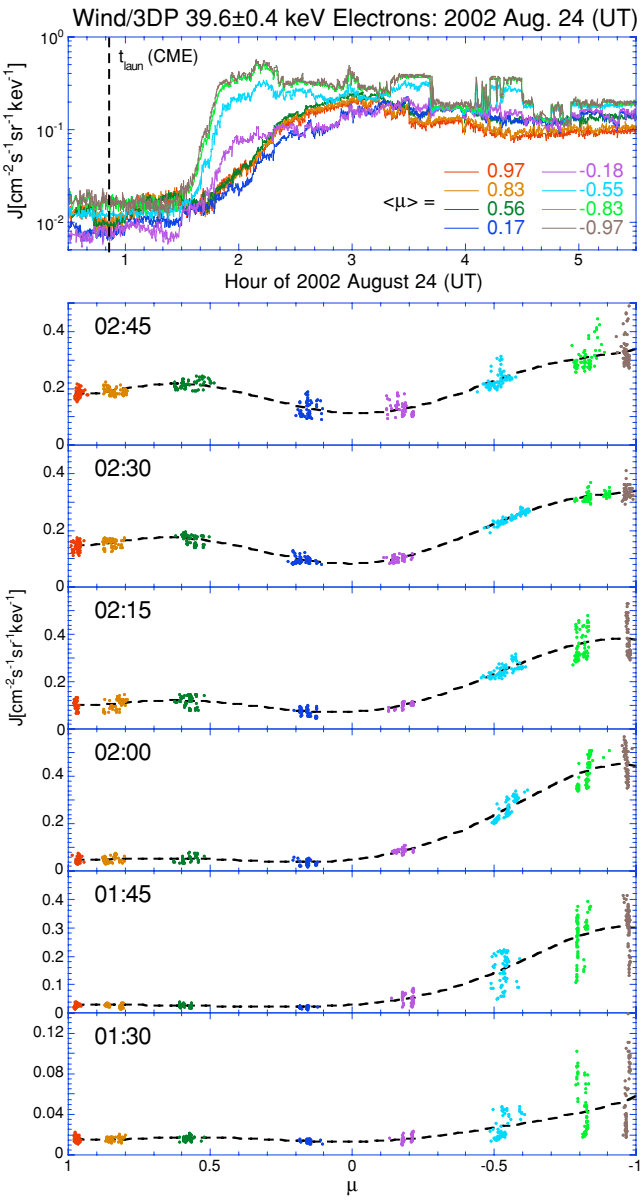

Figure 11. Same as Figure 2, but for the 2002 August 24 event, where the scattering-corrected electron intensity (J) is plotted after the subtraction of the background electron intensity estimated from the time period of 00:30–01:30 (UT), 2002 August 24. It should be emphasized that in all figures except this figure, the particle intensity data are plotted without background subtraction.

data (Figure 7), we take $\mu_m \sim 0.7$ for our further calculations. We hence obtain $l_m \sim 0.4$ (AU). Our deduced l_m is consistent with the estimated radial location of the leading edge of the preceding CME1 (∼1.3 AU).

3. DISCUSSION

3.1. Effect of Longitudinal Variation of Solar-wind Velocity

In Figure 9, we present the time profiles of the strength (B), latitude (θ_B), and longitude (ϕ_B) of IMF and the solar-wind speed (V_{sw}) deduced from *Wind* measurements over a 10-day interval for the September event. During the SEP onset phase (after t_{laun}(CME2)), the observed $\phi_B \sim 225°$ (the horizontal dashed line in the third panel) indicates that **B** was nearly perpendicular to the nominal Parker spiral direction. In addition, as shown in Figures 6 and 7 of Tan et al. (2007) during the onset phase the ion bulk flow velocity ($\mathbf{V}_F$) was sunward and eastward. Therefore, $\mathbf{V}_F$ was opposite to **B**, a scenario inconsistent with the cartoon shown in Figure 1 of Tan et al. (2008) based on constant V_{sw} assumption.

The IP shock driven by the preceding CME1 arrived at 1 AU at t_{obs}(Shock1), after which the solar-wind velocity rose to a peak of 580 km s^{-1}; then at t_{laun}(CME2) it decreased to 450 km s^{-1}. If the observed time variation of the solar-wind velocity mapped approximately to the longitudinal variation of the velocity along an IP field line (e.g., Ng 1987), then the frozen-in field line would have traveled outward at different radial velocities at different longitudes, resulting in the configuration for the field lines that passed through the *Wind* spacecraft at $\phi_B \sim 225°$ (Figure 9). This is also consistent with our deduced L_{0i} value traveled by first arriving particles from the Sun to 1 AU. The L_{0i} value is found to be greater than the length of the nominal Parker spiral (see Section 2.3). In addition, although $\mathbf{V}_F$ has a sunward component, solar particles are actually flowing eastward and away from the Sun. Therefore, the observed directions of $\mathbf{V}_F$ and **B** are consistent with the time variation of observed solar-wind velocity as mapped to a longitudinal variation on a field line. In Figure 1 of Tan et al. (2008), where the effect of solar-wind variation was not taken into account, the location of the magnetic mirror point is assumed to be near the nose of CME1. This is inconsistent with the field-line configuration in Figure 9, which would enhance the eastward convergence of the field lines on the eastern flank of the bulge, shifting the mirror point to the western flank of CME1 as inferred. Therefore, for the September event the bottom panel of Figure 9 should supersede the cartoon in Figure 1 of Tan et al. (2008), although the idealized cartoon ignores potential distortions due to the activity of other slow CMEs between the launch times of CME1 and CME2.

3.2. Discrimination Between Presence and Absence of the Boundary

Since the existence of the outer reflecting boundary would cause the reservoir effect that may enhance the intensity and duration of high-energy protons in a flux tube blocked by the boundary; identifying the presence of the boundary is important in space weather forecasting. Therefore, it is interesting to look for a condition by which we can discriminate between the presence and absence of the boundary.

We may hope to use energetic electron data to find such a condition in view of the high speed of the electrons. From Figure 2, it can be seen that during the early stage of the onset phase the reflected electrons appear without any enhancement at $\mu \sim 0$. This suggests that this feature—a strong reflected beam without enhancement at $\mu \sim 0$—can be used as a condition for deciding on the presence of a nearby reflecting boundary.

In addition to the existence of a boundary in the September event, in Tan et al. (2008) we also speculated on the presence and absence of a nearby boundary in the 2002 April 21 and 2002 August 24 events, respectively. Therefore, if the depression of electrons at $\mu \sim 0$ is the condition to detect the presence of a boundary, we should observe the depression of electrons at $\mu \sim 0$ in the April event, but not in the August event. Therefore, using a format similar to Figure 2, we plot Figures 10 and 11 for the April and August events, respectively. Because the velocity of 40 keV electrons is 2.7 AU hr^{-1}, we will concentrate on the first 1–2 hr after electron injection to examine the characteristic difference of observed electron pitch-angle distributions in these events.

In the April event, we indeed observed the enhancement of reflected electrons earlier than the arrival of $\mu \sim 0$ electrons.

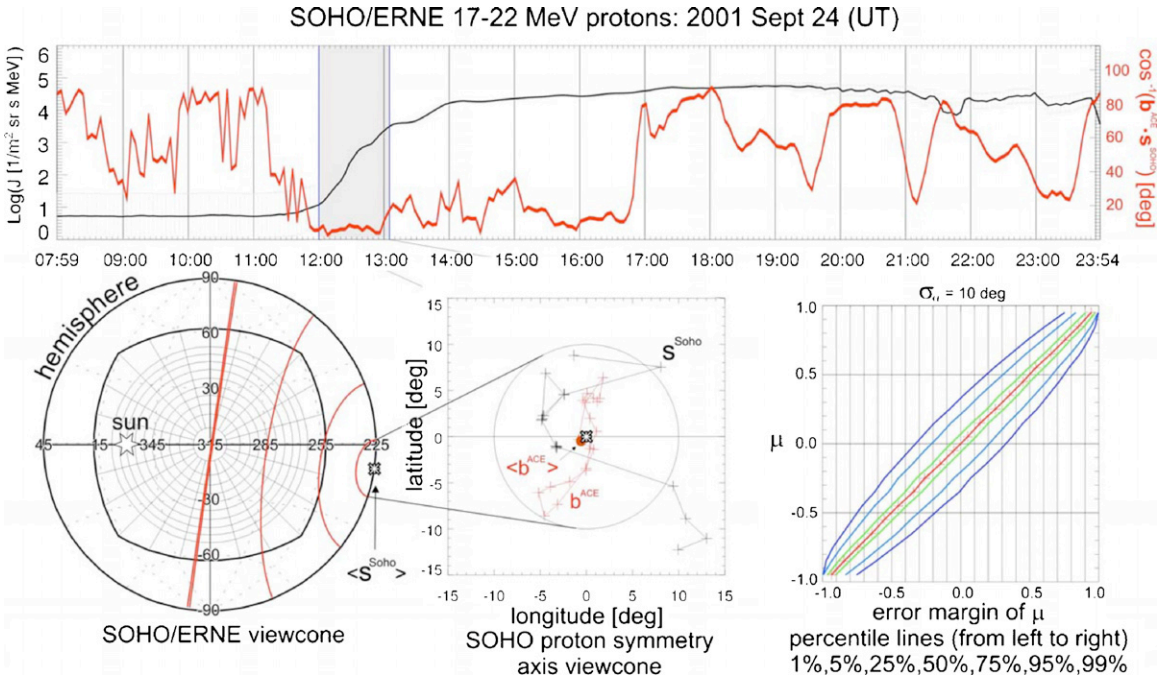

Figure 12. Comparison between the *ACE* magnetic field unit vector ($\mathbf{b}^{ACE}$) and *SOHO*/ERNE proton symmetric axis unit vector ($\mathbf{s}^{SOHO}$). Upper panel: the red and black lines express the angular distance δ between $\mathbf{b}^{ACE}$ and $\mathbf{s}^{SOHO}$ (i.e., $\delta = \cos^{-1}(\mathbf{b}^{\rm ACE} \cdot \mathbf{s}^{\rm SOHO})$) and proton intensity, respectively. The shaded region denotes the time period of 11:59–13:06 (UT), during which reflected protons were observed. Lower panel: the details of $\mathbf{b}^{ACE}$ and $\mathbf{s}^{SOHO}$ distributions inside the shaded region are given in the *SOHO* proton symmetric axis view cone shown in the central panel. The estimated error margin of μ is given in the right panel, where the percentile line indicates the percentage value of distribution mass coming before that line. The view-cone schematic of *SOHO*/ERNE 17–22 MeV protons is seen in the left panel.

In addition, from the top panel of Figure 10 it can be seen that the depression of $\mu \sim 0$ electrons lasted more than 4 hr, much longer than in the September event. More surprisingly, there was no intensity maximum of reflected electrons at $\mu \sim -0.7$ as seen in the September event. The intensity enhancement of reflected electrons continued as μ approached to -1, indicating $\alpha_{\rm loss} \sim 0$ or $B_m \rightarrow \infty$.

The $\alpha_{\rm loss}$ difference between the September and April events may be understandable in view of the characteristic difference of the reflecting boundaries between the two events. In fact, in the April event after the launch of the main CME (CME2) the *Wind* spacecraft was located inside a magnetic cloud (MC) having classical flux rope-like magnetic field structure (Burlaga et al. 1981; Klein & Burlaga 1982; Cane & Richardson 2003). The reduced turbulence inside the MC probably caused reduced electron scattering that would explain the extended duration of depression at $\mu \sim 0$. It is likely that a strong compression region exists within this MC at a shorter distance from the 1 AU observer. On the other hand, since a possible topology of MC is the magnetic bottle, inside which the magnetic field line is connected to the Sun at its both ends (Kahler & Reames 1991). When compared with the B value observed at 1 AU, we can assume $B \rightarrow \infty$ near the Sun and hence $\alpha_{\rm loss} \sim 0$ if the mirroring point were close to the Sun. Obviously, it is worthwhile to perform further examination on the April event, which may provide a possibility to explore MC topology by using the reflected electron distribution.

In contrast, the situation is different for the 2002 August event shown in Figure 11, where the background electron intensity estimated from the observations during 00:30–01:30 (UT), 2002 August 24 has been subtracted from the scattering-corrected electron intensity (J) data. From the figure, it can be seen that during the first 1 hr after electron injection there was no intensity peak of reflected electrons seen at $\mu > 0$.

As time elapsed all electron intensities at $\mu > 0$ presented a slight increase until the time interval of 02:30–03:00 (UT), during which a shallow dip of electron pitch-angle distributions developed near $\mu = 0$. While the dip may indicate some evidence of reflection in this event, it is extremely weak and delayed. The presence of a weak distant reflection with a substantial loss cone is nearly obscured by electron scattering. It appears, therefore, that to discriminate for a nearby reflecting boundary one must have both a strong reflected electron beam *and* a deep intensity depression at $\mu \sim 0$.

Anderson et al. (1981) observed the depression of 90° pitch-angle solar electrons in the 2–20 keV range. At even lower energies, Gosling et al. (2001) reported the depression of 90° pitch-angle solar-wind suprathermal electrons. In both works, the depression of 90° pitch-angle electrons in the open field-line setting is explained as the adiabatic mirroring effect due to the high field strength beyond 1 AU as suggested in the present work. Nevertheless, it should be emphasized that at low energies the beam of reflected electrons would continuously appear during a period of a few hours, making it difficult to estimate their characteristic times. In contrast, at higher energies as examined in this work the observed solar particles are related to the occurrence of a specific SEP event. Thus, the arrival times at 1 AU of both incident and reflected electrons can be determined based on onset time analysis. Hence, we are often able to estimate parameters characterizing the boundary and compare them with IMF and solar-wind measurements.

Therefore, if the finding in Figures 2, 10, and 11 could be verified by further observations, a strong reflected electron beam with a deep intensity depression at $\mu \sim 0$ would be a good evidence to discriminate for the presence and absence of a nearby reflecting boundary when electron scattering is not too large. The condition is attractive because the electron reflection occurs at the early stage during the onset phase, leaving enough

time to forecast the occurrence of high-intensity and long-duration SEP events.

4. SUMMARY

We have examined the 2001 September 24 SEP event for evidence of the presence of a nearby outer reflecting boundary of SEPs. Properties of this event are contrasted with those of the events of 2002 April 21 and August 24. Our main findings are as follows.

1. At the early stage during the onset phase of the September event by using both 25–400 keV electron data from the *Wind*/3DP sensor, and 20–40 MeV proton data from the *SOHO*/ERNE sensor, we observed a well separated reflected particle beam with a deep intensity depression at $\mu \sim 0$, confirming the presence of a nearby outer reflecting boundary of SEPs.
2. The outer reflecting boundary of SEPs in the September event has the following characteristics: the distance from the observer at 1 AU to the magnetic mirror point is ∼0.4 AU; the $|\mu|$ value of reflected particle peak intensity is ∼0.7.
3. A deep depression of electrons at $\mu \sim 0$, separating incident and reflected beams, was observed in the 2001 September 24 and 2002 April 21 events, in which the presence of a nearby boundary is confirmed. A delayed reflected particle beam was much less prominent in the 2002 August 24 event, in which the absence of a nearby boundary is expected. As a result, a strong reflected beam with a deep depression of electron intensity at $\mu \sim 0$ could be a strong evidence (with minimal scattering) to discriminate for the presence of a boundary.
4. A loss cone was observed in the 2001 September 24 event, but not in the 2002 April 21 event, which occurred inside an MC, implying the possibility of using the reflected electron distribution to explore the topology of the MC.
5. In the 2001 September 24 event as the peak intensity of reflected particles increased with time, the width of their pitch-angle distribution also increased. As a result, the $\mu \sim 0$ region was predominantly filled by reflected particles.

We gratefully acknowledge data provided by the NASA/Space Physics Data Facility (SPDF) CDAWeb, *Wind*/3DP Data Center, and *SOHO* LASCO CME catalog, which is generated and maintained at the CDAW Data Center by NASA and the Catholic University of America in cooperation with the Naval Research Laboratory. We thank K. Ogilvie, R. Lin, A. Zambo, and X. Shao for their support of this work. We also thank the anonymous reviewer for his/her valuable comments. L.C.T. is supported in part by NASA grant NNX09AF28G, D.V.R. is supported in part by NASA grant NNX08AQ02G. C.K.N. is supported under NASA grants LWS04–0000-0076 and SHP04–0016-0024. L.W. is supported in part by NASA grant NNX08AE34G.

APPENDIX

UNCERTAINTY IN PROTON PITCH-ANGLE DISTRIBUTIONS DUE TO THE LACK OF MAGNETIC FIELD MEASUREMENT ABOARD *SOHO* SPACECRAFT

In Figure 1, the unit vector $\mathbf{s}^{SOHO}$ (the white cross), along the symmetry axis of *SOHO* proton pitch-angle distribution, is close to $\mathbf{b}^{ACE}$ (the red star), the unit vector along the magnetic field measured by *ACE* spacecraft, indicating that the bulk-flow direction of SEPs follows the magnetic field. This observation is consistent with our finding in Tan et al. (2007), where by using the *Wind*/MFI and *Wind*/LEMT observations we confirmed that during the onset phase of the 2001 September 24 event the bulk-flow direction of SEPs, at lower energy, followed the local magnetic field (see Figures 6 and 7 in Tan et al. 2007). Therefore, during the onset phase of the September event, the real *SOHO* magnetic field direction can be approximated by $\mathbf{s}^{SOHO}$. The $\mathbf{s}^{SOHO}$ value is estimated by polynomial fitting of proton pitch-angle distributions. Normally, a polynomial of degree 3 is used in fitting procedure. In addition, an iteration technique is introduced in order to increase the resultant accuracy of the fitting, which is roughly 3° in angular space. See Saloniemi (2004) for the details of fitting procedure.

During other phases in the September event, however, the real *SOHO* magnetic field direction may not be approximated by $\mathbf{s}^{SOHO}$, because the contribution of solar-wind convective anisotropy may not be field aligned. Thus, the magnetic field measurement by the *ACE* or *Wind* spacecraft must be used to determine the magnetic field direction provided those spacecraft positions are close enough to *SOHO*. Since during the September event period the GSE *X*-coordinate of *SOHO* was 242 R_E, which was close to that of *ACE* (224 R_E) but greater than that of *Wind* (88 R_E), the magnetic field vector $\mathbf{b}^{ACE}$ measured by *ACE* was used in further analysis.

We compare $\mathbf{b}^{ACE}$ with $\mathbf{s}^{SOHO}$ in order to determine the uncertainty of the *SOHO* proton pitch-angle distributions due to the lack of on-site magnetic field measurements. Over the time interval of 08:00–24:00 (UT), 2001 September 24, the angular difference δ between $\mathbf{b}^{ACE}$ and $\mathbf{s}^{SOHO}$ (i.e., $\delta = \cos^{-1}(\mathbf{b}^{\rm ACE} \cdot \mathbf{s}^{\rm SOHO})$) is shown as the red line in the upper panel of Figure 12. We find that $\delta < 10°$ during the onset phase of the September event in the time interval 11:59–13:06 (UT) (shaded region, see Figure 4) used for the study of the proton reflection process.

In the lower part of Figure 12, we further examine the details of $\mathbf{b}^{ACE}$ and $\mathbf{s}^{SOHO}$ distributions in the shaded region. The central panel shows the *SOHO* proton symmetry axis view cone centered at $\langle \mathbf{s}^{SOHO} \rangle$, the $\mathbf{s}^{SOHO}$ vector averaged in the shaded time period. In this view-cone schematic, the black and red crosses represent the sampled $\mathbf{s}^{SOHO}$ and $\mathbf{b}^{ACE}$ data, respectively. From the $\mathbf{s}^{SOHO}$ data ensemble, the calculated standard deviation is $\sigma_s = 8.^\circ5$. In addition, from the $\mathbf{b}^{ACE}$ data ensemble, the calculated angular difference δ_{bs} between $\langle \mathbf{b}^{ACE} \rangle$ and $\langle \mathbf{s}^{SOHO} \rangle$ is $0.^\circ85$ and the standard deviation is $\sigma_b = 5.^\circ0$. Since the SEP bulk-flow direction follows the local magnetic field, the $\mathbf{s}^{SOHO}$ data ensemble can sample the real *SOHO* magnetic field direction, but may have larger instrumental error σ_s ($>\sigma_b$) because of imperfect bulk-flow analysis (e.g., the assumption of rotational symmetry). In contrast, the $\mathbf{b}^{ACE}$ data ensemble does not sample the real *SOHO* magnetic field direction. They may have a systematic error in tracing the *SOHO* magnetic field direction because of the position difference between the *SOHO* and *ACE* spacecraft. Fortunately, in view of the fact that δ_{bs} is much less than σ_s or σ_b the systematic error would be small. Therefore, the angular difference between the magnetic field direction measured by *ACE* spacecraft ($\mathbf{b}^{ACE}$) and the real *SOHO* magnetic field direction should be $\leqslant \sigma_s$, because the uncertainty of the real *SOHO* magnetic field direction is mainly determined by σ_s. We hence recognize that the uncertainty of the pitch angle α, $\sigma_\alpha \sim \sigma_s = 8.^\circ5$.

As the uncertainty of the pitch-angle cosine $\sigma_\mu = \sin(\alpha)\,\sigma_\alpha$, with $\sigma_\alpha \sim \sigma_s \sim 10^\circ$, the estimated error margin of μ can be found from the right panel, where the percentile line indicates the percentage of distribution coming before that line. The range between 5% and 95% (1% and 99%) lines approximates the $\pm\ 2\sigma$ ($\pm 3\sigma$) limit in Gaussian statistics. For example, at $\mu = 0.75$, the $\pm 2\sigma$ ($\pm 3\sigma$) limit is $\mu = 0.60$–0.85 (0.50–0.93).

REFERENCES

Anderson, K. A., McFadden, J. P., & Lin, R. P. 1981, Geophys. Res. Lett., 8, 831
Bieber, J. W., et al. 2002, ApJ, 567, 622
Burlaga, L. F., et al. 1981, J. Geophys. Res., 86, 6673
Cane, H. V., & Richardson, I. G. 2003, J. Geophys. Res., 108, 1156
Desai, M. I., et al. 2003, ApJ, 588, 1149
Desai, M. I., et al. 2004, ApJ, 611, 1156
Dröge, W. 2000, ApJ, 537, 1073
Efron, B., & Tibshirani, R. 1991, Science, 253, 390
Gosling, J. T., Skoug, R. M., & Feldman, W. C. 2001, Geophys. Res. Lett., 28, 4155
Kahler, S. W., & Ragot, B. R. 2006, ApJ, 646, 634
Kahler, S. W., & Reames, D. V. 1991, J. Geophys. Res., 96, 9419
Klein, L. W., & Burlaga, L. F. 1982, J. Geophys. Res., 87, 613
Lin, R. P., et al. 1995, Space Sci. Rev., 71, 125
Lintunen, J., & Vainio, R. 2004, A&A, 420, 343
McGuire, R. E., von Rosenvinge, T. T., & McDonald, F. B. 1986, ApJ, 301, 938.
Mewaldt, R. A., et al. 2003, in Proc. 28th Int. Cosmic Ray Conf. Vol. 6 (Tokyo: Universal Academy Press), 3313
Ng, C. K. 1987, Solar Phys., 114, 165
Press, W. H., et al. 1989, Numerical Recipes (Cambridge: Cambridge Univ. Press), 202
Reames, D. V. 1999, Space Sci. Rev., 90, 413
Reames, D. V. 2009, ApJ, 693, 812
Reames, D. V., Barbier, L. M., & Ng, C. K. 1996, ApJ, 466, 473
Reames, D. V., & Ng, C. K. 2002, ApJ, 577, L59
Roelof, E. C., et al. 1992, Geophys. Res. Lett., 19, 1243
Saiz, A., et al. 2005, ApJ, 626, 1131
Saloniemi, O. 2004, Directional Distributions of Particle Flows Emanating from the Sun as Measured by *SOHO*/ERNE (in Finnish), Master's thesis, Turku University
Tan, L. C., Reames, D. Y., & Ng, C. K. 2007, ApJ, 661, 1297
Tan, L. C., Reames, D. Y., & Ng, C. K. 2008, ApJ, 678, 1471
Tan, L. C., et al. 1992, J. Geophys. Res., 97, 1597
Torsti, et al. 1995, Sol. Phys., 162, 505
Tylka, A. J., & Lee, M. A. 2006, ApJ, 646, 1319
Tylka, A. J., et al. 2003, in Proc. 28th Int. Cosmic Ray Conf. Vol. 6 (Tokyo: Universal Academy Press), 3305
Tylka, A. J., et al. 2005, ApJ, 625, 474
Tylka, A. J., et al. 2006, ApJS, 164, 536
von Rosenvinge, T. T., et al. 1995, Space Sci. Rev., 71, 155
Wang, L., et al. 2006, Geophys. Res. Lett., 33, L03106